Structure and flexibility of the extracellular region of the PirB receptor

Received for publication, June 13, 2018, and in revised form, January 14, 2019 Published, Papers in Press, January 23, 2019, DOI 10.1074/jbc.RA118.004396

Hedwich C. Vlieg, Eric G. Huizinga, and Bert J. C. Janssen[1]

From Crystal and Structural Chemistry, Bijvoet Center for Biomolecular Research, Department of Chemistry, Faculty of Science, Utrecht University, 3584 CH Utrecht, The Netherlands

Edited by Roger J. Colbran

Murine paired immunoglobulin receptor B (PirB) and its human ortholog leukocyte immunoglobulin-like receptor B2 (LILRB2) are widely expressed inhibitory receptors that interact with a diverse set of extracellular ligands and exert functions ranging from down-regulation of immune responses to inhibition of neuronal growth. However, structural information that could shed light on how PirB interacts with its ligands is lacking. Here, we report crystal structures of the PirB ectodomain; the first full ectodomain structure for a LILR family member, at 3.3–4.5 Å resolution. The structures reveal that PirB's six Ig-like domains are arranged at acute angles, similar to the structures of leukocyte immunoglobulin-like receptor (LILR) and killer-cell immunoglobulin-like receptor (KIR). We observe that this regular arrangement is followed throughout the ectodomain, resulting in an extended zigzag conformation. In two out of the five structures reported here, the repeating zigzag is broken by the first domain that can adopt two alternative orientations. Quantitative binding experiments revealed a 9 μM dissociation constant for PirB–myelin-associated glycoprotein (MAG) ectodomain interactions. Taken together, these structural findings and the observed PirB—MAG interactions are compatible with a model for intercellular signaling in which the PirB extracellular domains, which point away from the cell surface, enable interaction with ligands in *trans*.

Mouse Paired immunoglobulin-like receptor B (PirB),[2] also named leukocyte immunoglobulin-like receptor subfamily B member 3 (LILRB3), is a promiscuous type I transmembrane receptor with diverse tissue-dependent functions, ranging from immune response modulation, hematopoietic stem cell consolidation to central nervous system plasticity regulation. To exert its cellular functions a diverse set of cell surface-expressed and secreted ligands interact with the PirB ectodomain.

This work was supported by Netherland Organization for Scientific Research (NWO) VIDI Grant 723.012.002 and NWO Grant 01.80.104.00. The authors declare that they have no conflicts of interest with the contents of this article.

This article contains Figs. S1–S7.

The atomic coordinates and structure factors (codes 6GRQ, 6GRS, and 6GRT) have been deposited in the Protein Data Bank (http://wwpdb.org/).

[1] To whom correspondence should be addressed. Tel.: 0031-30-2532866; E-mail: b.j.c.janssen@uu.nl.

[2] The abbreviations used are: PirB, paired immunoglobulin-like receptor B; LILRB2, leukocyte immunoglobulin-like receptor subfamily B member 3; MHC-I, major histocompatibility complex class I; MAI, myelin-associated inhibitor; MAG, myelin-associated glycoprotein; SPR, surface plasmon resonance; r.m.s., root mean square; MR, molecular replacement.

PirB is a member of the LILR family; LILRs are receptors for major histocompatibility complex class I (MHC-I) proteins and modulate the strength of immune responses by stimulatory (LILRAs) or inhibitory (LILRBs) signaling (1, 2). PirB is a functional ortholog of human LILRB2. As such, it is used as a mouse model to study LILRB2 function.

PirB is expressed on various types of hematopoietic cells, where it down-regulates activation and differentiation. For example, through interaction with MHC-I molecules, PirB inhibits B-cell (3) and mast cell activation (4). Furthermore, through interaction with secreted angiopoietin-like proteins, PirB down-regulates blood platelet activation (5) and is involved in maintaining the stemness of hematopoietic stem cells (6).

Unlike the other LILRB family members, PirB and LILRB2 are also expressed in neurons, where they are involved in restricting synaptic plasticity and neuronal regeneration. PirB and MHC-I regulate synaptic plasticity in the visual cortex (7, 8). In addition, PirB is found to be involved in Alzheimer's disease as a receptor for β-amyloid (9). PirB and LILRB2 are also receptors for a group of ligands called the myelin-associated inhibitors (MAIs) (10). These MAIs are Nogo (11, 12), myelin-associated glycoprotein (MAG) (13), and oligodendrocyte-myelin glycoprotein (OMgp) (14). In the healthy central nervous system this inhibitory signaling helps to balance the neuronal plasticity needed for basic brain function such as learning and memory (15). However, on injury this inhibition prevents neuronal regeneration, leading to permanent damage to neuronal circuits (16).

PirB is a type I transmembrane protein with a domain organization that is typical for the LILR protein family (17). The extracellular segment is predicted to consist of six tandem Ig-like domains, referred to as D1–D6. The Ig-like domains are connected to a transmembrane helix by a short linker that is predicted to be disordered and *O*-linked glycosylated. The intracellular tail contains three immunoreceptor tyrosine-based inhibitor motives. Upon activation of the receptor through ligand binding, tyrosines in these motives are phosphorylated by Src family kinases (18, 19). The phosphotyrosines recruit Src homology domain 2-containing phosphatase 1 or 2 (SHP-1/2), which mediate further downstream signaling (20–22).

PirB shares a high sequence homology with LILR proteins and, in particular, with its human ortholog LILRB2, with which it has an overall sequence identity of 52% for the extracellular

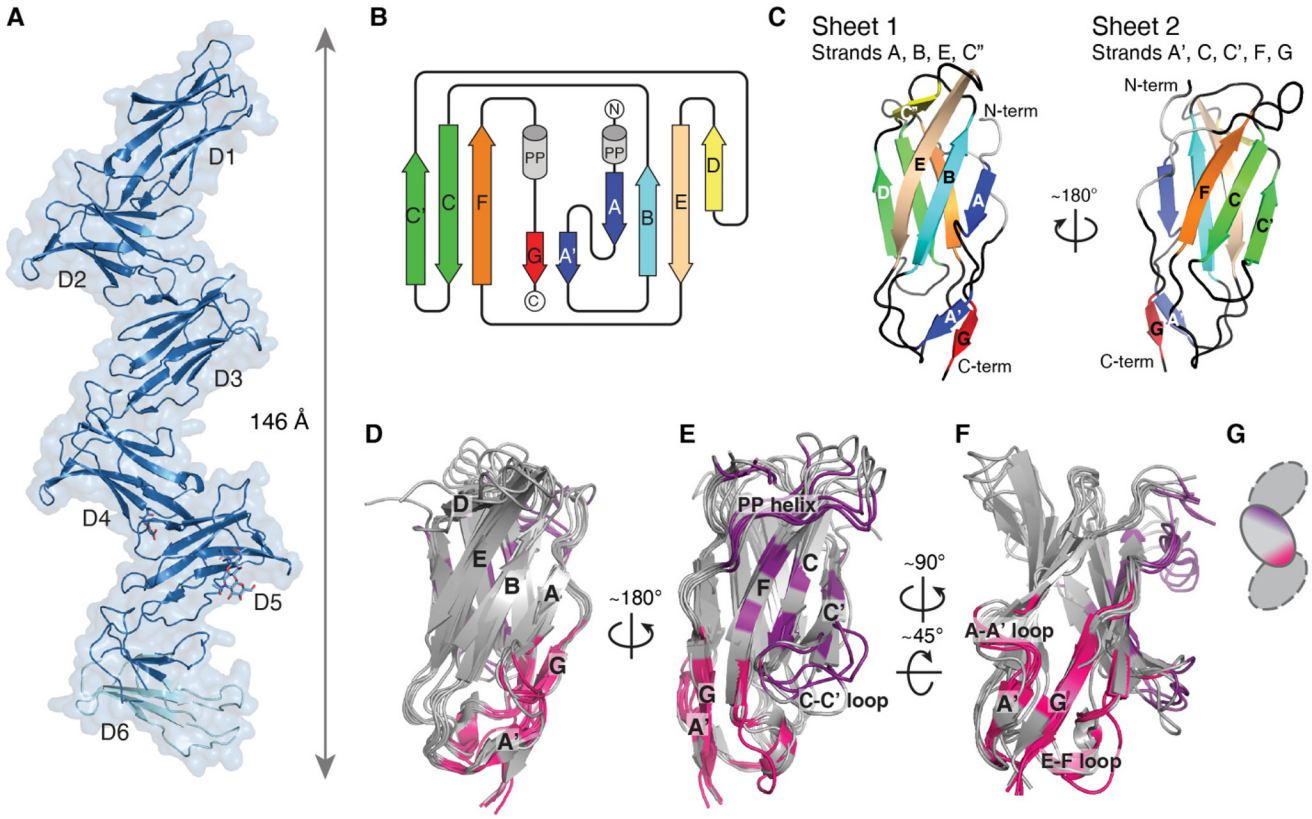

Figure 1. Crystal structure of PirB$_{1-6}$ reveals a semi-rigid zigzag of tandem Ig-like domains. *A,* the PirB ectodomain forms an elongated structure with a repeating zigzag of Ig-like domains D1 to D6. Glycans are shown in stick representation. The model depicted is from PirB$_{cryst1}$; the *light blue* part of D6 is missing in the density, and has been extended here for viewing purposes using D6 of PirB$_{cryst2-B}$. *B,* topology diagram for D2; β-sheets (*arrows*) and polyproline helices (*gray cylinders*) are indicated. Topology diagrams for the other domains can be found in Fig. S1. *C,* ribbon drawing of D2, using the same color scheme as in *B*. *D–F,* overlay of all six of PirB's Ig-like domains (D1 to D5 from PirB$_{cryst1}$ and D6 from PirB$_{cryst2}$) illustrates the close structural similarity between domains and domain interfaces. Residues involved in interactions with the previous domain (forming the C-terminal face of the interface) are colored *purple*, and residues involved in interactions with the next domain (forming the N-terminal face of the interface) are shown in *pink*. This color scheme is illustrated in the cartoon (*G*).

Ig-like domains. Instead of the six Ig-like domains for mouse PirB, the human LILRB2 ectodomain consists of only four Ig-like domains. The first and third domain of PirB are most similar to the first domain of LILRB2 (35 and 43% sequence identity, respectively), whereas the second and fourth domains of PirB are most similar to the second domain of LILRB2 (56 and 43% sequence identity, respectively). The fifth and sixth domain of PirB are most similar to the third and fourth domain of LILRB2 (64 and 57% sequence identity, respectively). Although mouse PirB and human LILRB2 differ in domain number, they interact with a similar set of ligands and have similar functions (1, 6, 10)

Despite the functional importance of PirB, there is no structural information available. To date, the only known structures for LILR family members consist of two consecutive Ig-like domains. For example, two partial ectodomain structures have been published for LILRB2, one of the first two domains, D1–D2 (23), and one of the last two domains, D3–D4 (24). Insight in the structural features of PirB will aid understanding of how the protein is able to interact with such diverse ligands and trigger signaling to carry out its diverse range of functions.

Here we present the crystal structure of the PirB ectodomain and investigate its interactions with the extracellular segment of the MAI MAG. The six Ig-like domains of PirB are arranged in an extended repeating zigzag arrangement. The PirB N-terminal domain, D1, has positional flexibility and adopts three alternative orientations in which the angle between domains D1 and D2 varies from 75° to 315°. Using surface plasmon resonance (SPR) experiments we show that the dissociation constant for the PirB–MAG ectodomain interaction is 9 μM. The extended conformation of PirB may enable *trans*-cellular interaction with ligands, such as MAG and MHC-I, to induce intercellular signaling.

Results

PirB adopts an extended zigzag structure

The crystal structure of the PirB ectodomain containing all 6 Ig-like domains (PirB$_{1-6}$) reveals an extended zigzag conformation with multiple orientations for the N-terminal Ig-like domain (Fig. 1 and Fig. S1). The PirB$_{1-6}$ structure was determined in three crystal forms, denoted PirB$_{cryst1}$, PirB$_{cryst2}$, PirB$_{cryst3}$, with maximum resolutions of 3.3, 3.4, and 4.5 Å, respectively (Table 1). In two of the crystal forms, PirB$_{cryst2}$ and PirB$_{cryst3}$, the asymmetric unit contains two monomers, resulting in a total of five unique structures. The six tandem Ig-like domains are arranged in a zigzag shape, with only minor deviations between the five structures (Fig. 2, *A–C*, and Fig. S2). From tip to tip (Tyr-104–Cα to Ser-536–Cα), the structure measures 146 Å in the extended conformation found in

Table 1
Crystallographic data collection and refinement statistics

	$PirB_{cryst1}$	$PirB_{cryst2}$	$PirB_{cryst3}$
Data collection			
Beamline	DLS I04	SLS PX	SLS PX-I (1.0000 Å)[a]
Wavelength (Å)	0.9795	1.0000	ESRF ID23-1 (0.9686 Å)[a]
Space group	$P4_122$	$P2_1$	$P2_1$
Cell dimensions			
a, *b*, *c* (Å)	106.4 106.4 217.9	54.7 185.3 99.1	67.3 127.1 144.1
α, β, γ (°)	90 90 90	90 105.6 90	90 103.4 90
Resolution (Å)	53.19 − 3.30 (3.56 − 3.30)	52.69 − 3.40 (3.63 − 3.40)	70.07 − 4.50 (4.67 − 4.50)
No. reflections	19,634 (3,949)	25,778 (4,683)	13,858 (1,273)
R_{merge}	0.277 (2.767)	0.108 (0.824)	0.226 (0.907)
$I/\sigma I$	8.2 (1.5)	6.9 (1.8)	4.0 (1.6)
Completeness (%)	100 (100)	98.8 (99.2)	98.9 (98.0)
Redundancy	22.3 (22.5)	3.2 (3.2)	3.5 (3.5)
$CC_{1/2}$	0.998 (0.542)	0.949 (0.586)	0.960 (0.594)
Refinement			
Chains in asymmetric unit	1	2	2
R_{work}/R_{free}	0.248 / 0.295	0.256 / 0.307	0.313 / 0.339
No. non-H atoms			
Protein	4,222	9,167	9,264
Ligand/ion	42	42	42
B-factors (Å^2)			
Protein	128	139	244
Ligand/ion	182	212	254
R.m.s. deviations			
Bond lengths (Å)	0.003	0.003	0.008
Bond angles (°)	0.79	0.68	1.22
Ramachandran most favored (%)	94.10	95.75	94.45
Ramachandran outliers (%)	0.20	0.52	1.62
Molprobity score	2.14	1.76	2.09
Protein Data Bank code	6GRQ	6GRS	6GRT

[a] Diffraction data for this crystal were collected at two different beamlines and combined to form one dataset, see "Experimental procedures" for details.

$PirB_{cryst1}$. Glycans are observed in four of the six predicted *N*-linked glycosylation sites (Asn-338, -479, -500, and- 531), in at least one of the five structures. In $PirB_{cryst1}$ domain D6 is partially disordered; residues 528–549 and 567–593 are not visible in the electron density and were omitted from the model. The best-defined structure for domain 6 is observed in the second monomer (chain B) of $PirB_{cryst2}$ ($PirB_{cryst2\text{-}B}$), therefore this structure is used for the analysis of D6 outlined below, additionally this structure is used to supplement the $PirB_{1-6}$ structure shown in Fig. 1*A*.

The six Ig-like domains are composed of two antiparallel β-sheets, linked together by a disulfide bridge. The six domains are topologically similar to each other (Fig. 1, *B–F*, and Fig. S1), and to the Ig-like domains of KIR and other LILR proteins (23–36). β-Sheet 1 comprises strands A, B, D, and E and sheet 2 comprises strands A′, C, C′, F, and G. As is often seen in LILR and KIR family members, the A–A′ strand is shared between the two β-sheets. Additionally, there is a polyproline helix before β-strands A and G and a 3_{10}-helix in the E–F loop. These secondary structure elements are not present in all domains, for instance, D1, D3, and D6 lack β-strand D, in D5 and D6 the G and A′ strands are unraveled, and in D2 and D6 the 3_{10}-helix is missing. Moreover, β-strand G is very short in D2 and it does not interact with β-strand F, leaving a separate parallel β-sheet composed of strands A′ and G. Despite the differences in secondary structure elements, the three-dimensional structures of all six Ig-like domains are very similar; in $PirB_{cryst1}$ they have an average r.m.s. deviation on C_α's of just 1.6 ± 0.3 Å (Fig. 1, *D–F*).

Domain interfaces

Consecutive Ig-like domains interact with each other through topologically equivalent interfaces (Fig. 1, *D–F*) that are also observed in the two or three domain containing structures for LILR and KIR proteins (23–35). In PirB this "canonical" domain interface is repeated five times, resulting in the observed extended zigzag shape (Fig. 1*A*). In each interface, the most N-terminal domain contributes residues of the A′ strand, G strand, and E–F loop (Fig. 1*F*), whereas the C-terminal side of the interface (located on the following domain) is centered on β-sheet 2 and comprises the F, C, and C′ β-strands, the C–C′ loop, and the polyproline helix preceding strand G (*purple* in Fig. 1*E*). These interactions leave sheet 1 (strands A, B, D, and E) and the N-terminal tip of the domain (strand D and connecting loops and the B–C loop) available for interactions with ligands.

The domain interfaces are stabilized by hydrophobic interactions, hydrogen bonds, and salt bridges. On average, the total surface area buried in an interface is 1088 ± 158 Å^2. All interfaces, except the D4–D5 interface, have a hydrogen bonding network between residues in strand G or loop E–F on the N-terminal domain to residues in loop F–G on the C-terminal domain. Additionally, in each interface a salt bridge or hydrogen bond is formed between a residue in strand G (or in loop A–A′ in D1) and a residue in strand C′, located at the edge of the interface. Interaction through this canonical interface results in an acute angle between consecutive domains. The orientation is slightly different for each domain pair, with interdomain angles ranging from 62° to 79° (Fig. 2, *A–C*, and Fig. S2).

This range of observed interdomain angles is in line with structures of other LILR and KIR proteins (23–36). Structural comparison of PirB with partial structures available for LILRB2 (23, 24), PirB's closest human homologue, yields r.m.s. deviations that follow the trend expected from sequence identity. PirB domains 5–6 are most similar to LILRB2 domains 3–4

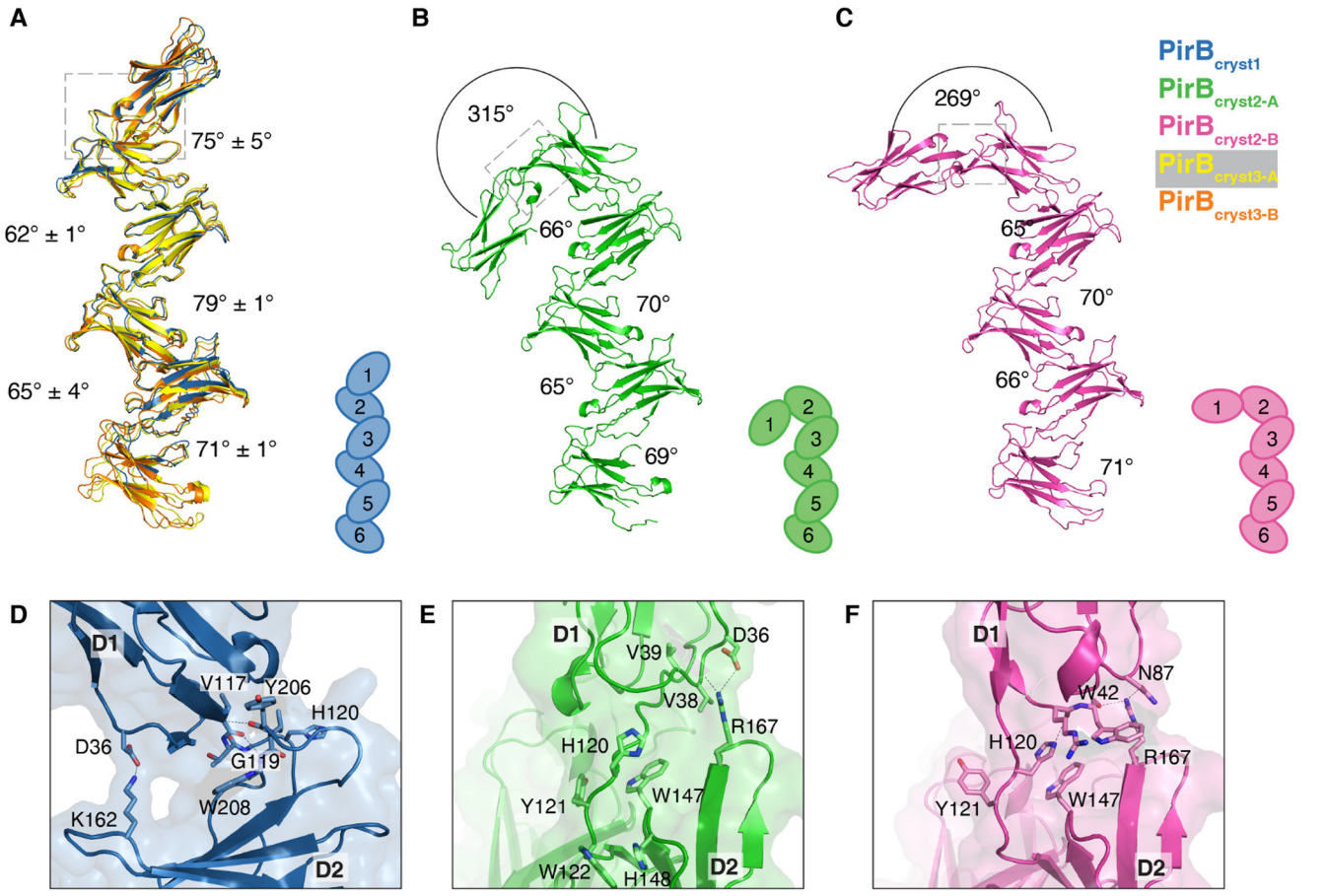

Figure 2. PirB D1 can deviate from the canonical zigzag and adopts three distinct orientations. *A–C,* the five unique PirB structures from three crystal forms are shown. *A,* PirB chains A (*yellow*) and B (*orange*) from $PirB_{cryst3}$ are overlaid with $PirB_{cryst1}$ (*blue*), these three structures show the same regular zigzag conformation. *B* and *C,* the $PirB_{cryst2}$ chains A (*green*) and B (*pink*) show strikingly different angles between D1 and D2. *D–F,* close-up of the interface between D1 and D2 for each of the three distinct orientations of D1, the enlarged area is indicated by a *dashed-line box* in *B–D*. The side chains of selected residues are shown in stick representation. For clarity, the two structures from $PirB_{cryst3}$ are not included in *D*.

(60% sequence identity, 1.1 Å r.m.s. deviation in $PirB_{cryst2\text{-}B}$). LILRB2 domains 1 and 2 are most closely related to PirB domains 1–2 (46% sequence identity, 2.2 Å r.m.s. deviation in $PirB_{cryst1}$) and PirB domains 3–4 (44% sequence identity, 2.1 Å r.m.s. deviation in $PirB_{cryst1}$).

PirB domain D1 can adopt three different orientations

In two of our PirB structures D1 and D2 do not interact via the canonical interface, resulting in two PirB conformations that deviate from the regular zigzag described above (Fig. 2, *A–C,* and Fig. S3). In both monomers in $PirB_{cryst2}$ D1 is bend over to the other side of D2, predominantly rotating around the Trp-122 C–Cα bond, resulting in an interdomain angle of 315° in chain A and an angle of 269° in chain B (Fig. 2, *B* and *C*).

The three distinct D1 orientations give rise to three different D1–D2 interfaces (Fig. 2, *D–F*). The canonical D1–D2 interface, seen in $PirB_{cryst1}$, is smaller than the other canonical interfaces, it has an average total buried surface area of 903 ± 51 Å^2 *versus* 1145 ± 107 Å^2 for the other domain interfaces. The canonical D1–D2 interface consists of a hydrophobic core centered around Trp-208 in strand G of D2, together with a hydrogen bonding network between the backbones of Val-117 and Gly-119 in strand G of D1, and Tyr-206 and Trp-208 in strand G of D2 (Fig. 2*D*). The domain orientation is further stabilized by a salt bridge between Asp[36] in the A–A′ loop of D1, and Lys-162 in strand C′ on D2.

The two noncanonical interfaces are even smaller, with only 542 Å^2 total buried surface area in monomer A and 436 Å^2 in monomer B. The noncanonical interfaces on D1 partially overlap with the canonical interface. In monomer A, this interface comprises strand A′, loop E–F, and the domain linker; all but one (Val-39) of the D1 residues are also involved in the canonical interface (Fig. 2*E*). In monomer B, the interface on D1 comprises loops A′–B and E–F, and the domain linker (Fig. 2*F*). On D2 the noncanonical interfaces are very different from the canonical one. In chain A, Trp-147 in the B–C loop replaces Trp-208 as the central residue in the hydrophobic interface (Fig. 2*E*). Moreover, residues in the linker region between the domains contribute to the interface; His-120 and Tyr-121 line the interface and Trp-122 interacts through ring stacking with His-148 in loop B–C on D2. In chain B, the hydrophobic part of the interface is formed by Trp-42 in loop A′–B of D1, and Trp-147 in loop B–C of D2 (Fig. 2*F*). Both noncanonical interfaces are further stabilized by salt bridges and hydrogen bonds, although the hydrogen bonding network is not as extensive as the one seen in the canonical D1–D2 interfaces.

In summary, our crystal structures show three distinct orientations for PirB D1. Chain B in $PirB_{cryst2}$ seems to represent an intermediate state between the canonical conformation and the conformation of $PirB_{cryst2}$ chain A. On the other hand, the main body of the protein, D2–D6, shows very little conformational variation. Taken together, the PirB structures indicate that whereas there is limited flexibility between domains D2–D6, a range of orientations is possible for D1.

PirB self-association

$PirB_{cryst1}$ and $PirB_{cryst2}$ reveal dimers with a common intermolecular interface that may represent a PirB *cis* dimer (Fig. 3). The interface has a total buried surface area of 3531 Å^2 in $PirB_{cryst1}$ and 3708 Å^2 in $PirB_{cryst2}$, whereas the area of the second largest interfaces in these crystals are 1991 and 1609 Å^2, respectively. In the third crystal form this dimer is not observed; here the largest interface is 2087 Å^2. The putative dimerization interface consists of two patches. The first patch starts at the C-terminal tip of D2 and continues across D3 to the N-terminal tip of D4. The second patch comprises residues at the C-terminal tip of D4 and the N-terminal tip of D5. D1 is not involved in this putative dimerization interface; therefore, the interface is not affected by the observed mobility of this domain.

PirB shows self-association in SPR (Fig. S4). Although, homointeractions can be detected by SPR they cannot be quantified using this technique as self-association of ligands coupled on the chip surface compete with analyte binding. Despite this, both the crystal structures and the SPR data indicate that PirB has propensity to self-associate.

Ligand binding

Ligand interaction is critical to PirB's role as an extracellular receptor. To verify the interaction of the PirB ectodomain for ligand binding, SPR experiments were performed for PirB's known binding partner MAG (Figs. S5 and S6). C terminally biotinylated $PirB_{1-6}$ was immobilized at three different densities on a streptavidin-coated SPR chip, to probe interactions with increasing concentrations of the extracellular segment of MAG in the mobile phase. The entire extracellular MAG segment, containing five extracellular Ig-like domains (MAG_{1-5}), was used. MAG_{1-5}–$PirB_{1-6}$ binding was found to have a K_D of 9 ± 2.9 μM (Fig. S6).

Discussion

PirB is a versatile receptor that binds to numerous, structurally varied ligands. We have solved the structure of PirB's ectodomain in three conformations and performed binding experiments to gain insight into PirB-ligand binding. What sets the PirB ectodomain structure apart from other structures of LILR and KIR family members is that it is the largest of its kind to be elucidated and it is the only reported KIR/LILR structure with multiple orientations for one of its domains.

The six Ig-like domains that make up PirB's ectodomain are arranged in a regular zigzag repeat. Interestingly, the first domain can break this regular pattern and adopt multiple orientations. In our crystal structures three distinct orientations are observed for PirB D1. In all three crystal forms the D1 domain is involved in crystal packing and this may stabilize

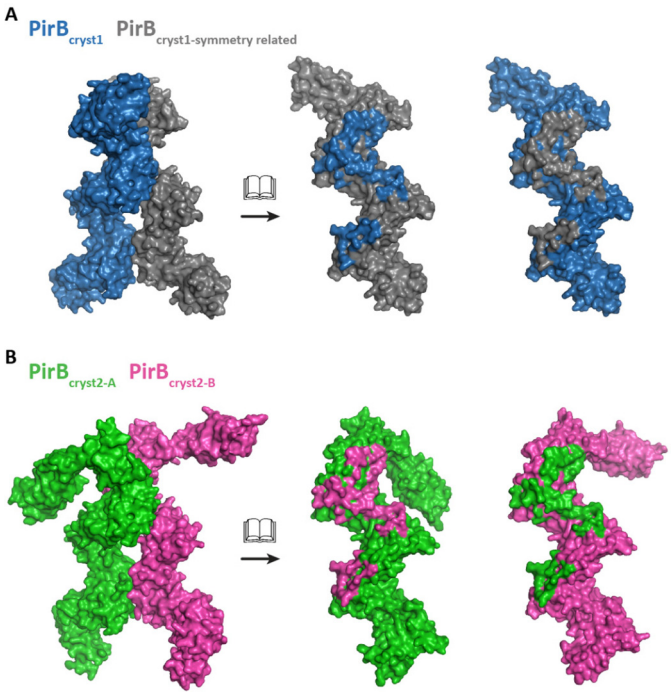

Figure 3. The same PirB dimer is observed in two crystal forms. Dimer and open book representation with a footprint indicating the interacting residues for (*A*) $PirB_{cryst1}$ and (*B*) $PirB_{cryst2}$. Note that the dimer in $PirB_{cryst1}$ is generated by a crystallographic 2-fold axis and the *gray* monomer is therefore identical to the *blue* monomer.

conformations of PirB that are only sparsely populated in solution. The conformations in $PirB_{cryst1}$ and $PirB_{cryst2\text{-}A}$ seem to represent the extremes in a range of conformations, whereas $PirB_{cryst2\text{-}B}$ represents an intermediate state between the two. To our knowledge flexibility of one of the Ig-like domains has not been reported for any of the LILR or KIR family members. Furthermore, there are no indications of such flexibility in the structures for LILR and KIR family members. This is surprising, as, at first glance, the PirB D1–D2 interface is very similar to the D1–D2 interfaces of other LILR family members, by comparing the sequences or the available structures.

The conformational variability in PirB may be explained by the size of the interface and a number of residues unique to PirB. The canonical D1–D2 interface is less extensive than the other canonical interfaces in PirB, with an average total buried surface area of 903 ± 51 Å^2 instead of 1145 ± 107 Å^2 for the other interfaces. However, it is in the same range as the D1–D2 interface in other LILR structures, where the total buried surface area is 839 ± 37 Å^2 (23, 34–36). Moreover, the three-dimensional organization of the interface is very well conserved between the LILRs and PirB. On closer inspection, four residues unique to PirB, but with important roles in the three different interfaces (Fig. 2, *D–F*) stand out; His-120 and Trp-42, -122, and -147. His-120 is part of the linker region between D1 and D2 and points outward into the solvent in the canonical structure. The corresponding residue in other LILR family members (human LILRs A1, A2, A3, A4, B1, B2, B3, and B4 and mouse LILRB4), is an alanine that does not participate in the D1–D2 interface, or a phenylalanine (human LILRs A5, A6, and B5 and chimpanzee LILR A6 and B5), that engages in extensive hydrophobic interactions with domain 1. As His-120 is bulky, unlike

the much smaller alanine, and is not able to contribute to the interface with hydrophobic interactions like phenylalanine, it might destabilize the $PirB_{cryst1}$ D1–D2 interface. The three tryptophans unique to PirB (42, 122, and 147) are not involved in the canonical interface, instead they provide hydrophobic patches for D1 interaction in the noncanonical orientations. Because of the location of Trp-147 in loop BC, which is of variable length, the corresponding residues in other LILR family members can only be determined by structural comparison. In LILRs with published structures the corresponding residues are glutamine or arginine, with extended hydrophilic side chains that are consistent with exposure to the solvent. For Trp-42 the corresponding residue in other LILR family members is always an arginine and for Trp-122 the corresponding residues are either hydrophilic (Glu, Ser, Asn) or small (Pro, Ile, Ala). These corresponding residues would not be able to interact with D1 in the same manner as Trp-42, -122, or -147. In conclusion, three tryptophans that are unique to PirB provide alternate interfaces for D1–D2 interaction and, together with His-120, may promote conformational mobility of D1.

Our crystal structures provide evidence for PirB dimerization, and SPR data also indicate that $PirB_{1-6}$ has a propensity for self-association. Although our experimental data on PirB dimerization are not conclusive, oligomerization (*e.g.* dimerization) could be part of the signaling mechanism in (some of) PirB's roles as a receptor when expressed on the cell surface. Nonetheless, to our knowledge, dimerization has not been documented to have a functional role for any of the LILR family members, nor for the related KIR proteins. Also, there is no evidence for dimerization in the (partial) structures of LILR and KIR proteins.

$PirB_{1-6}$ is separated from the cell surface by a 19-amino acid linker that may confer flexibility to the orientation of PirB with respect to the membrane. Therefore, whereas the maximum distance that the six Ig-like domains can span in the extended PirB conformation is 146 Å, it is not clear if PirB projects that far from the membrane. If PirB adopts a dimer conformation as observed in $PirB_{cryst1}$ and $PirB_{cryst2}$ the orientation relative to the membrane becomes much more restricted. A PirB dimer in the extended zigzag conformation ($PirB_{cryst1}$) would protrude 130 Å from the plane defined by the most membrane-proximal tips of the protein (Fig. S7). For the noncanonical orientations of D1, this distance is less; 100 Å in the fully flipped conformation ($PirB_{cryst2\text{-}A}$) and 120 Å in the intermediate state ($PirB_{cryst2\text{-}B}$).

Neuronal PirB interacts with MAIs, expressed on oligodendrocytes, in *trans*. Although interactions of MAIs with the Nogo Receptor (NgR) have been well studied (37, 38), less is known about binding of these proteins to PirB. Binding affinities of 14 nM have been reported for Fc-tagged MAG to PirB (10), but this interaction is most likely enhanced by artificially dimerizing MAG. Indeed, weaker interactions of 33 μM have been reported for binding of untagged MAG to PirB (39) although in their experiments the maximum concentration of MAG used, 3 μM, is too low for accurate affinity determination. Using higher MAG concentrations we obtain an affinity of 9 μM for the MAG–PirB interaction.

There are no crystal structures available of complexes involving MAG and PirB to provide additional clues to how these proteins might interact (Fig. 4*A*). Structures are available of LILR family members in complex with MHC-I loaded with a (viral) peptide. The LILR–MHC-I *trans* binding mode is highly conserved among all studied complexes (40). As a member of the LILR family, PirB is likely to display the same binding mode to form complexes with MHC-I (Fig. 4*B*). Interestingly, PirB would only be able to bind MHC-I complexes in the extended zigzag conformation; in the noncanonical conformations, seen in $PirB_{cryst2}$, D1 would clash with the MHC-I complex. PirB dimerization as observed in $PirB_{cryst1}$ and $PirB_{cryst2}$ on the other hand would not interfere with MHC-I binding.

In conclusion, our data reveal that the extracellular segment of PirB is extended and that PirB has a propensity to self-associate. The dimerization mode revealed in the crystal structures of $PirB_{1-6}$ is compatible with dimer formation of full-length transmembrane PirB on the cell surface in *cis*, but the importance of PirB dimerization for signaling has not been investigated further. In full-length PirB the mobile N-terminal domain D1 is likely positioned furthest away from the cell surface, poised for interaction with ligands on other cells. Possibly, the mobility of D1 contributes to its ability to interact with a diverse set of binding partners. Taken together, our structural and interaction data are compatible with a model for intercellular signaling in which PirB has an extended conformation on the cell surface to enable interaction with ligands in *trans* (Fig. 4).

Experimental procedures

Cloning of constructs

The soluble ectodomain constructs for PirB and MAG were generated using polymerase chain reaction (PCR). The templates and construct boundaries are listed in Table 2. All constructs were subcloned into pUPE107.30 (U-Protein Express) (C-terminal His_6 tag) using BamHI/NotI restriction sites. For SPR experiments the original $PirB_{1-6}$ construct was subcloned into pUPE107.62, a vector containing a C-terminal His_6 tag for purification and a C-terminal biotin acceptor peptide tag for biotinylation.

Expression and purification

The soluble ectodomain constructs (in vector pUPE107.30) were expressed by transient transfection in HEK293-ES cells (U-Protein Express) and grown in FreeStyle 293 Expression Medium (Thermo Fisher). HEK293-ES is a cell line that lacks the *N*-acetylglycosaminyltransferase I enzyme and therefore produces proteins with short, homogeneous oligomannose glycans (41). After 6 days, cells are spun down (10 min at 1000 × *g*) and the medium was harvested. The medium was concentrated 10-fold and diafiltrated against IMAC binding buffer (500 mM NaCl, 50 mM Hepes pH 7.8) using a Quixstand benchtop system (GE Healthcare). Cell debris was removed by centrifugation (30 min at 9500 × *g*). The protein was purified from the cleared concentrate by Ni-affinity chromatography on a 5-ml HiTrap column (GE Healthcare) followed by SEC on a Superdex 200 column (GE Healthcare) equilibrated with SEC buffer (150 mM NaCl, 25 mM Hepes, pH 7.5). The purified protein was concentrated using a spin concentrator with the appropriate MWCO, snap frozen in liquid nitrogen, and stored at −80 °C until use.

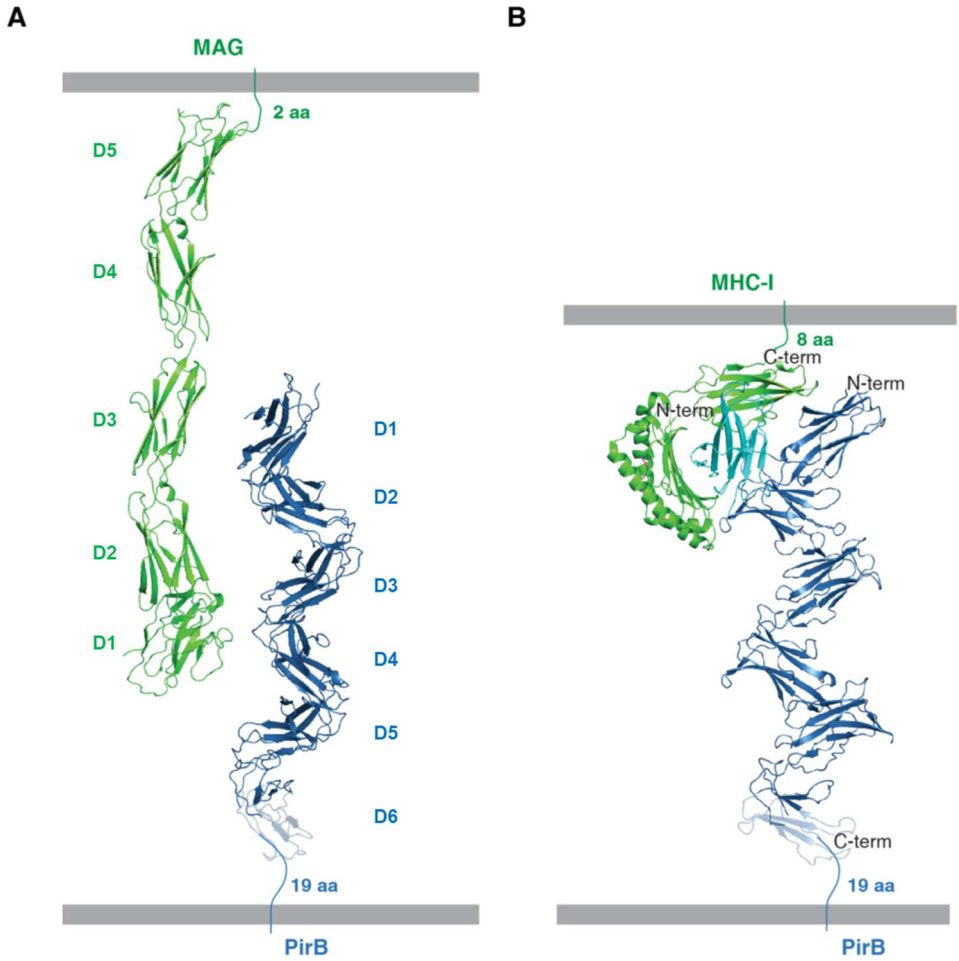

Figure 4. Models for intercellular interaction of PirB with two ligands, MAG and MHC-I. *A,* crystal structures for MAG (PDB code 5LF5) (52) and PirB are shown in ribbon representation. *B,* model for the PirB MHC-I complex based on the structure of LILRB2 in complex with HLA-G (PDB code 2DYP) (23). HLA-G is composed of an α chain (*green*) and β2-microglobulin (*cyan*) and is loaded with a peptide (*pink*). In *A* and *B* the PirB structure shown is from $PirB_{cryst1}$; the semi-transparent part of D6 is missing in the density, and has been extended here for viewing purposes using D6 of $PirB_{cryst2\text{-}B}$. The number of amino acids between the structured part and the membrane attachment site is indicated near each linker.

Table 2
Ectodomain constructs

Construct	Residues (Uniprot)	Uniprot entry No.	Template
$PirB_{1-6}$	25–619	P97484	IMAGE clone 4488338
MAG_{1-5}	20–508	P20917	IMAGE clone 40039200

$PirB_{1-6}$ for SPR was expressed in HEK293-ES cells (U-Protein Express), in small 4-ml cultures. To allow *in vivo* biotinylation of these constructs, the cells were co-transfected with the *Escherichia coli* BirA biotin ligase and the cell medium was supplemented with 25 μg/ml of biotin. After 6 days, the medium was harvested as described above and diluted 10-fold with IMAC binding buffer. The protein was purified from the diluted medium by batch binding to Ni-Sepharose beads (GE Healthcare). After incubation at room temperature for 2 h, the beads were transferred to spin columns (Thermo Fisher) and washed 4 times with binding buffer, followed by elution with 50 μl of binding buffer supplemented with 200 mM imidazole.

Crystallization and data collection

Crystals of $PirB_{1-6}$ were grown at 20 °C using the hanging drop vapor diffusion method and a concentration of 9 to 10 mg/ml of $PirB_{1-6}$. $PirB_{cryst1}$, in space group $P4_122$, was obtained against a reservoir solution of 1.1 M LiCl, 14% PEG 6000, 0.1 M citric acid buffer, pH 5.5. A dataset to 3.3 Å resolution was collected at Diamond light source beamline I04 (wavelength 0.9795 Å, temperature 100 K). $PirB_{cryst2}$, in space group $P2_1$, was obtained against a reservoir solution of 1.2 M LiCl, 12% PEG 6000, 0.1 M citric acid buffer, pH 5.5. A dataset to 3.4 Å resolution was collected at Swiss light source beamline PX-I (wavelength 1.0000 Å, temperature 100 K). $PirB^{cryst\text{-}3}$, also in space group $P2_1$, was obtained against a reservoir solution of 14.6% polyacrylate 5100 sodium salt and 0.07 M Tris, pH 8.0. An incomplete dataset to 4.5 Å was collected at Swiss light source beamline PX-I (wavelength 1.0000 Å, temperature 100 K). The missing degrees were collected at ESRF beamline ID23-1 (wavelength 0.9686 Å, temperature 100 K). The two datasets were merged in AIMLESS and further processed as described below.

Structure solution and refinement

The data were integrated using iMOSFLM (42) or XDS (43), followed by scaling and merging using the AIMLESS pipeline (44). In brief, the strategy for solving and refinement of the structures was as follows; the three structures were solved in the

order in which the datasets were collected (first $PirB_{cryst3}$, then $PirB_{cryst2}$, and finally $PirB_{cryst1}$). Each time, the previously solved and partially refined structure was used as a molecular replacement (MR) model for the next dataset. Resulting in the "best" PirB structure from $PirB_{cryst1}$. To improve the other two structures, the domains of the refined $PirB_{cryst1}$ structure were placed back in density for $PirB_{cryst2}$ and $PirB_{cryst3}$ followed by further refinement to yield the structures reported here.

The structure for $PirB_{cryst3}$ was solved with MR in Phaser (45), using structures of LILRA5 (35) and LILRB2 (24) as MR models. The structure was refined using iterative rounds of manual building in Coot (46) and refinement in REFMAC 5 (47). The resulting structure was used as a model for MR to solve the structure of $PirB_{cryst2}$ with Phaser. To prevent bias in the domain orientations, single domains were used as MR models. The resulting structure was refined in Coot and REFMAC. The same domain-by-domain approach was used to solve the structure from $PirB_{cryst1}$, with $PirB_{cryst2}$ as a MR model. The new structure was refined in REFMAC and phenix.refine (48) and manual model building in Coot.

To improve the structure from $PirB_{cryst2}$, D1–D5 of this structure were substituted with D1–D5 from $PirB_{cryst1}$. This was done by individually superimposing the domains, followed by extensive refinement in REFMAC, phenix.refine, and manual model building in Coot. A similar approach was used to improve the structure from $PirB_{cryst3}$, domains from the higher resolution $PirB_{cryst1}$ (D1 and D2–D5) and $PirB_{cryst2}$ (D6) were used to rebuild the structure. To avoid overfitting of the low resolution $PirB_{cryst3}$ structure, refinement was kept to a minimum. After an initial round of rigid body refinement (one body per domain) in phenix.refine, a limited number of adjustments were made in Coot. Namely, the missing domain connections were added; sugars were added where they were visible in the density; His-120 and Tyr-121, which are Ramachandran outliers in the model because of a crystal contact, were fixed; and loop 170–178, which is displaced in the $PirB_{cryst3}$ structure because of a crystal contact, was modeled in the visible density using the corresponding region in $PirB_{cryst2\text{-}A}$ as a template. After this model building the structure was subjected to one round of jelly body refinement in REFMAC and one more round of rigid body refinement in phenix.refine.

Structure analysis

The domain interfaces for all five unique monomers as well as the dimer interfaces were analyzed using the PISA server (49). Angles between Ig-like domains were determined from the angles between the largest principle axes of these domains. Glycosylation predictions were preformed using the NetNGlyc 1.0 Server and the NetOGlyc 4.0 Server (50). Structure r.m.s. deviations were calculated in gesamt (51), using the Cα atoms for alignment. All figures of the structures were generated using PyMol (DeLano Scientific LLC).

Surface plasmon resonance

SPR experiments were performed on an MX96 (IBIS Technologies), using a SensEye Sensor (IBIS Technologies) with a streptavidin-coated dextran matrix. Biotinylated $PirB_{1-6}$ was coupled to the chip as the SPR ligands using a Wasatch Microfluidics continuous flow microspotter. This method creates multiple spots, or regions of interest on the chip surface, each with a ligand density of choice. Purified analyte (MAG_{1-5} or $PirB_{1-6}$, Figs. S4 and S6) was flowed over the chip at a constant temperature of 25 °C in running buffer (150 mM NaCl, 20 mM Hepes, pH 7.2, 0.001% Tween 20). Equilibrium binding experiments were performed to measure the binding affinities of MAG to PirB. Using the analyte in a concentration range of 0.8–108 μM for MAG_{1-5}.

Data processing was started in SprintX (IBIS Technologies), where the data were blanked once, using reference spots close to the regions of interest. The data were then zeroed before each injection of analyte, and exported to Scrubber (BioLogic). In Scrubber the amount of bound MAG_{1-5} was determined when equilibrium is reached at the end of the association phase (Fig. S6). A saturation curve was fitted with a 1:1 Langmuir binding model in GraphPad Prism to determine the maximum analyte binding (B_{max}) and equilibrium binding constant (K_D) of MAG_{1-5}–$PirB_{1-6}$ interaction.

Author contributions—H. C. V. and B. J. J. data curation; H. C. V., E. G. H., and B. J. J. formal analysis; H. C. V., E. G. H., and B. J. J. validation; H. C. V. investigation; H. C. V., E. G. H., and B. J. J. visualization; H. C. V. and B. J. J. methodology; H. C. V. writing-original draft; H. C. V., E. G. H., and B. J. J. writing-review and editing; B. J. J. conceptualization; B. J. J. supervision; B. J. J. funding acquisition; B. J. J. project administration.

Acknowledgments—We thank the staff of European Synchrotron Radiation Facility beamline ID23-1, Diamond light source beamline I04, and Swiss light source beamline PX-I.

References

1. Hudson, L. E., and Allen, R. L. (2016) Leukocyte Ig-like receptors: a model for MHC class I disease associations. *Front. Immunol.* **7,** 281 Medline
2. Takai, T. (2005) Paired immunoglobulin-like receptors and their MHC class I recognition. *Immunology* **115,** 433–440 CrossRef Medline
3. Maeda, A., Scharenberg, A. M., Tsukada, S., Bolen, J. B., Kinet, J. P., and Kurosaki, T. (1999) Paired immunoglobulin-like receptor B (PIR-B) inhibits BCR-induced activation of Syk and Btk by SHP-1. *Oncogene* **18,** 2291–2297 CrossRef Medline
4. Masuda, A., Nakamura, A., Maeda, T., Sakamoto, Y., and Takai, T. (2007) Cis binding between inhibitory receptors and MHC class I can regulate mast cell activation. *J. Exp. Med.* **204,** 907–920 CrossRef Medline
5. Fan, X., Shi, P., Dai, J., Lu, Y., Chen, X., Liu, X., Zhang, K., Wu, X., Sun, Y., Wang, K., Zhu, L., Zhang, C. C., Zhang, J., Chen, G. Q., Zheng, J., and Liu, J. (2014) Paired immunoglobulin-like receptor B regulates platelet activation. *Blood* **124,** 2421–2430 CrossRef Medline
6. Zheng, J., Umikawa, M., Cui, C., Li, J., Chen, X., Zhang, C., Huynh, H., Kang, X., Silvany, R., Wan, X., Ye, J., Cantó, A. P., Chen, S. H., Wang, H. Y., Ward, E. S., and Zhang, C. C. (2012) Inhibitory receptors bind ANGPTLs and support blood stem cells and leukaemia development. *Nature* **485,** 656–660 CrossRef Medline
7. Syken, J., Grandpre, T., Kanold, P. O., and Shatz, C. J. (2006) PirB restricts ocular-dominance plasticity in visual cortex. *Science* **313,** 1795–1800 CrossRef Medline
8. Bochner, D. N., Sapp, R. W., Adelson, J. D., Zhang, S., Lee, H., Djurisic, M., Syken, J., Dan, Y., and Shatz, C. J. (2014) Blocking PirB up-regulates spines and functional synapses to unlock visual cortical plasticity and facilitate recovery from amblyopia. *Sci. Transl. Med.* **6,** 258ra140 CrossRef Medline
9. Kim, T., Vidal, G. S., Djurisic, M., William, C. M., Birnbaum, M. E., Garcia, K. C., Hyman, B. T., and Shatz, C. J. (2013) Human LilrB2 is a β-amyloid

receptor and its murine homolog PirB regulates synaptic plasticity in an Alzheimer's model. *Science* **341,** 1399–1404 CrossRef Medline
10. Atwal, J. K., Pinkston-Gosse, J., Syken, J., Stawicki, S., Wu, Y., Shatz, C., and Tessier-Lavigne, M. (2008) PirB is a functional receptor for myelin inhibitors of axonal regeneration. *Science* **322,** 967–970 CrossRef Medline
11. Chen, M. S., Huber, A. B., van der Haar, M. E. D., Frank, M., Schnell, L., Spillmann, A. A., Christ, F., and Schwab, M. E. (2000) Nogo-A is a myelin-associated neurite outgrowth inhibitor and an antigen for monoclonal antibody IN-1. *Nature* **403,** 434–439 CrossRef Medline
12. GrandPré, T., Nakamura, F., Vartanian, T., and Strittmatter, S. M. (2000) Identification of the Nogo inhibitor of axon regeneration as a Reticulon protein. *Nature* **403,** 439–444 CrossRef Medline
13. McKerracher, L., David, S., Jackson, D. L., Kottis, V., Dunn, R. J., and Braun, P. E. (1994) Identification of myelin-associated glycoprotein as a major myelin-derived inhibitor of neurite growth. *Neuron* **13,** 805–811 CrossRef Medline
14. Kottis, V., Thibault, P., Mikol, D., Xiao, Z. C., Zhang, R., Dergham, P., and Braun, P. E. (2002) Oligodendrocyte-myelin glycoprotein (OMgp) is an inhibitor of neurite outgrowth. *J. Neurochem.* **82,** 1566–1569 CrossRef Medline
15. Baldwin, K. T., and Giger, R. J. (2015) Insights into the physiological role of CNS regeneration inhibitors. *Front. Mol. Neurosci.* **8,** 23 Medline
16. Boghdadi, A. G., Teo, L., and Bourne, J. A. (2018) The involvement of the myelin-associated inhibitors and their receptors in CNS plasticity and injury. *Mol. Neurobiol.* **55,** 1831–1846 CrossRef Medline
17. Kubagawa, H., Burrows, P. D., and Cooper, M. D. (1997) A novel pair of immunoglobulin-like receptors expressed by B cells and myeloid cells. *Proc. Natl. Acad. Sci. U.S.A.* **94,** 5261–5266 CrossRef Medline
18. Ho, L. H., Uehara, T., Chen, C.-C., Kubagawa, H., and Cooper, M. D. (1999) Constitutive tyrosine phosphorylation of the inhibitory paired Ig-like receptor PIR-B. *Proc. Natl. Acad. Sci.* **96,** 15086–15090 CrossRef Medline
19. Zhang, H., Meng, F., Chu, C. L., Takai, T., and Lowell, C. A. (2005) The Src family kinases Hck and Fgr negatively regulate neutrophil and dendritic cell chemokine signaling via PIR-B. *Immunity* **22,** 235–246 CrossRef Medline
20. Bléry, M., Kubagawa, H., Chen, C. C., Vély, F., Cooper, M. D., and Vivier, E. (1998) The paired Ig-like receptor PIR-B is an inhibitory receptor that recruits the protein-tyrosine phosphatase SHP-1. *Proc. Natl. Acad. Sci. U.S.A.* **95,** 2446–2451 CrossRef Medline
21. Maeda, A., Kurosaki, M., Ono, M., Takai, T., and Kurosaki, T. (1998) Requirement of SH2-containing protein tyrosine phosphatases SHP-1 and SHP-2 for paired immunoglobulin-like receptor B (PIR-B)-mediated inhibitory signal. *J. Exp. Med.* **187,** 1355–1360 CrossRef Medline
22. Berg, K. L., Carlberg, K., Rohrschneider, L. R., Siminovitch, K. A., and Stanley, E. R. (1998) The major SHP-1-binding, tyrosine-phosphorylated protein in macrophages is a member of the KIR/LIR family and an SHP-1 substrate. *Oncogene* **17,** 2535–2541 CrossRef Medline
23. Shiroishi, M., Kuroki, K., Rasubala, L., Tsumoto, K., Kumagai, I., Kurimoto, E., Kato, K., Kohda, D., and Maenaka, K. (2006) Structural basis for recognition of the nonclassical MHC molecule HLA-G by the leukocyte Ig-like receptor B2 (LILRB2/LIR2/ILT4/CD85d). *Proc. Natl. Acad. Sci. U.S.A.* **103,** 16412–16417 CrossRef Medline
24. Nam, G., Shi, Y., Ryu, M., Wang, Q., Song, H., Liu, J., Yan, J., Qi, J., and Gao, G. F. (2013) Crystal structures of the two membrane-proximal Ig-like domains (D3D4) of LILRB1/B2: alternative models for their involvement in peptide-HLA binding. *Protein Cell* **4,** 761–770 CrossRef Medline
25. Fan, Q. R., Mosyak, L., Winter, C. C., Wagtmann, N., Long, E. O., and Wiley, D. C. (1997) Structure of the inhibitory receptor for human natural killer cells resembles haematopoietic receptors. *Nature* **389,** 96–100 CrossRef Medline
26. Snyder G. A., Brooks, A. G., and Sun, P. D. (1999) Crystal structure of the HLA-Cw3 allotype-specific killer cell inhibitory receptor KIR2DL2. *Proc. Natl. Acad. Sci. U.S.A.* **96,** 3864–3869 CrossRef Medline
27. Maenaka, K., Juji, T., Stuart, D. I., and Jones, E. Y. (1999) Crystal structure of the human p58 killer cell inhibitory receptor (KIR2DL3) specific for HLA-Cw3-related MHC class I. *Structure* **7,** 391–398 CrossRef Medline
28. Moradi, S., Berry, R., Pymm, P., Hitchen, C., Beckham, S. A., Wilce, M. C., Walpole, N. G., Clements, C. S., Reid, H. H., Perugini, M. A., Brooks, A. G., Rossjohn, J., and Vivian, J. P. (2015) The structure of the atypical killer cell immunoglobulin-like receptor, KIR2DL4. *J. Biol. Chem.* **290,** 10460–10471 CrossRef Medline
29. Saulquin, X., Gastinel, L. N., and Vivier, E. (2003) Crystal structure of the human natural killer cell activating receptor KIR2DS2 (CD158j). *J. Exp. Med.* **197,** 933–938 CrossRef Medline
30. Graef, T., Moesta, A. K., Norman, P. J., Abi-Rached, L., Vago, L., Older Aguilar, A. M., Gleimer, M., Hammond, J. A., Guethlein, L. A., Bushnell, D. A., Robinson, P. J., and Parham, P. (2009) KIR2DS4 is a product of gene conversion with KIR3DL2 that introduced specificity for HLA-A* 11 while diminishing avidity for HLA-C. *J. Exp. Med.* **206,** 2557–2572 CrossRef Medline
31. Vivian, J. P., Duncan, R. C., Berry, R., O'Connor, G. M., Reid, H. H., Beddoe, T., Gras, S., Saunders, P. M., Olshina, M. A., Widjaja, J. M., Harpur, C. M., Lin, J., Maloveste, S. M., Price, D. A., Lafont, B. A., McVicar, D. W., Clements, C. S., Brooks, A. G., and Rossjohn, J. (2011) Killer cell immunoglobulin-like receptor 3DL1-mediated recognition of human leukocyte antigen B. *Nature* **479,** 401–405 CrossRef Medline
32. Ryu, M., Chen, Y., Qi, J., Liu, J., Fan, Z., Nam, G., Shi, Y., Cheng, H., and Gao, G. F. (2011) Lilra3 binds both classical and non-classical HLA class I molecules but with reduced affinities compared to lilrb1/lilrb2: structural evidence. *PLoS ONE* **6,** e19245 CrossRef Medline
33. Chapman, T. L., Heikema, A. P., West, A. P., Jr., and Bjorkman, P. J. (2000) Crystal structure and ligand binding properties of the D1D2 region of the inhibitory receptor LIR-1(ILT2). *Immunity* **13,** 727–736 CrossRef Medline
34. Cheng, H., Mohammed, F., Nam, G., Chen, Y., Qi, J., Garner, L. I., Allen, R. L., Yan, J., Willcox, B. E., and Gao, G. F. (2011) Crystal structure of leukocyte Ig-like receptor LILRB4 (ILT3/LIR-5/CD85k): a myeloid inhibitory receptor involved in immune tolerance. *J. Biol. Chem.* **286,** 18013–18025 CrossRef Medline
35. Shiroishi, M., Kajikawa, M., Kuroki, K., Ose, T., Kohda, D., and Maenaka, K. (2006) Crystal structure of the human monocyte-activating receptor, "Group 2" leukocyte Ig-like receptor A5 (LILRA5/LIR9/ILT11). *J. Biol. Chem.* **281,** 19536–19544 CrossRef Medline
36. Yang, Z., and Bjorkman, P. J. (2008) Structure of UL18, a peptide-binding viral MHC mimic, bound to a host inhibitory receptor. *Proc. Natl. Acad. Sci. U.S.A.* **105,** 10095–10100 CrossRef Medline
37. Schimmele, B., and Plückthun, A. (2005) Identification of a functional epitope of the Nogo receptor by a combinatorial approach using ribosome display. *J. Mol. Biol.* **352,** 229–241 CrossRef Medline
38. Zander, H., Reineke, U., Schneider-Mergener, J., and Skerra, A. (2007) Epitope mapping of the neuronal growth inhibitor Nogo-A for the Nogo receptor and the cognate monoclonal antibody IN-1 by means of the SPOT technique. *J. Mol. Recognit.* **20,** 185–196 CrossRef Medline
39. Matsushita, H., Endo, S., Kobayashi, E., Sakamoto, Y., Kobayashi, K., Kitaguchi, K., Kuroki, K., Söderhäll, A., Maenaka, K., Nakamura, A., Strittmatter, S. M., and Takai, T. (2011) Differential but competitive binding of Nogo protein and class I major histocompatibility complex (MHCI) to the PIR-B ectodomain provides an inhibition of cells. *J. Biol. Chem.* **286,** 25739–25747 CrossRef Medline
40. Willcox, B. E., Thomas, L. M., and Bjorkman, P. J. (2003) Crystal structure of HLA-A2 bound to LIR-1, a host and viral major histocompatibility complex receptor. *Nat. Immunol.* **4,** 913–919 CrossRef Medline
41. Reeves, P. J., Callewaert, N., Contreras, R., and Khorana, H. G. (2002) Structure and function in rhodopsin: High-level expression of rhodopsin with restricted and homogeneous *N*-glycosylation by a tetracycline-inducible *N*-acetylglucosaminyltransferase I-negative HEK293S stable mammalian cell line. *Proc. Natl. Acad. Sci. U.S.A.* **99,** 13419–13424 CrossRef Medline
42. Battye, T. G. G., Kontogiannis, L., Johnson, O., Powell, H. R., and Leslie, A. G. W. (2011) iMOSFLM: a new graphical interface for diffraction-image processing with MOSFLM. *Acta Crystallogr. Sect. D Biol. Crystallogr.* **67,** 271–281 CrossRef

43. Kabsch, W. (2010) Integration, scaling, space-group assignment and post-refinement. *Acta Crystallogr. Sect. D Biol. Crystallogr.* **66,** 133–144 CrossRef
44. Evans, P. R., and Murshudov, G. N. (2013) How good are my data and what is the resolution? *Acta Crystallogr. Sect. D Biol. Crystallogr.* **69,** 1204–1214 CrossRef
45. McCoy, A. J., Grosse-Kunstleve, R. W., Adams, P. D., Winn, M. D., Storoni, L. C., and Read, R. J. (2007) Phaser crystallographic software. *J. Appl. Crystallogr.* **40,** 658–674 CrossRef Medline
46. Emsley, P., Lohkamp, B., Scott, W. G., and Cowtan, K. (2010) Features and development of Coot. *Acta Crystallogr. Sect. D Biol. Crystallogr.* **66,** 486–501 CrossRef
47. Murshudov, G. N., Skubák, P., Lebedev, A. A., Pannu, N. S., Steiner, R. A., Nicholls, R. A., Winn, M. D., Long, F., and Vagin, A. A. (2011) REFMAC5 for the refinement of macromolecular crystal structures. *Acta Crystallogr. Sect. D Biol. Crystallogr.* **67,** 355–367 CrossRef
48. Headd, J. J., Echols, N., Afonine, P. V., Grosse-Kunstleve, R. W., Chen, V. B., Moriarty, N. W., Richardson, D. C., Richardson, J. S., and Adams, P. D. (2012) Use of knowledge-based restraints in phenix.refine to improve macromolecular refinement at low resolution. *Acta Crystallogr. Sect. D Biol. Crystallogr.* **68,** 381–390 CrossRef
49. Krissinel, E., and Henrick, K. (2007) Inference of macromolecular assemblies from crystalline state. *J. Mol. Biol.* **372,** 774–797 CrossRef Medline
50. Steentoft, C., Vakhrushev, S. Y., Joshi, H. J., Kong, Y., Vester-Christensen, M. B., Schjoldager, K. T., Lavrsen, K., Dabelsteen, S., Pedersen, N. B., Marcos-Silva, L., Gupta, R., Paul Bennett, E., Mandel, U., Brunak, S., Wandall, H. H., *et al.* (2013) Precision mapping of the human *O*-GalNAc glycoproteome through SimpleCell technology. *EMBO J.* **32,** 1478–1488 CrossRef Medline
51. Krissinel, E. (2012) Enhanced fold recognition using efficient short fragment clustering. *J. Mol. Biochem.* **1,** 76–85 Medline
52. Pronker, M. F., Lemstra, S., Snijder, J., Heck, A. J., Thies-Weesie, D. M., Pasterkamp, R. J., and Janssen, B. J. (2016) Structural basis of myelin-associated glycoprotein adhesion and signalling. *Nat. Commun.* **7,** 13584 CrossRef Medline